

Supplementary Materials for **The Rydberg constant and proton size from atomic hydrogen**

Axel Beyer, Lothar Maisenbacher,* Arthur Matveev, Randolph Pohl, Ksenia Khabarova,
Alexey Grinin, Tobias Lamour, Dylan C. Yost, Theodor W. Hänsch,
Nikolai Kolachevsky, Thomas Udem

*Corresponding author. Email: lothar.maisenbacher@mpq.mpg.de

Published 6 October 2017, *Science* **358**, 79 (2017)
DOI: 10.1126/science.aah6677

This PDF file includes:

- Materials and Methods
- Fig. S1
- Tables S1 to S3
- References

Materials and methods

1 Data acquisition and analysis

1.1 Data acquisition

Here we briefly review the experimental setup as depicted in Fig. 3 in the main text. Excitation of the $2S_{1/2}^{F=0}$ state takes place by Doppler-free two-photon excitation of the $1S_{1/2}^{F=0}$ - $2S_{1/2}^{F=0}$ transition using a preparation laser at 243 nm. The line width of this excitation is ~ 2 kHz (full width at half maximum (FWHM)) and is limited by time-of-flight broadening (1). Because this line width is much smaller than the 621 MHz laser detuning necessary to drive the $1S_{1/2}^{F=1}$ - $2S_{1/2}^{F=1}$ transition by Doppler-free two-photon excitation, the $2S_{1/2}^{F=1}$ states are only populated by Doppler-sensitive two-photon excitation. This leads to a negligible population of approx. 3×10^{-7} in each of the three $2S_{1/2}^{F=1}$ states relative to the population in the $2S_{1/2}^{F=0}$ state, because only a small number of atoms are in the velocity class that is resonant with this transition. The atoms then travel from the 1S-2S excitation region to the 2S-4P excitation region, where they interact with the two counter-propagating beams of the spectroscopy laser at 486 nm. Detection of the 2S-4P fluorescence only takes place after the production of 2S atoms has been discontinued at time $\tau = 0$, i.e. the 1S-2S excitation light has been blocked by a chopper wheel running at 160 Hz. At an excitation light intensity of about 1.4 W/m^2 (0.6 W/m^2) per direction of the spectroscopy laser (beam waist $w_0 = 1.85 \text{ mm}$), on average about 30% of the atoms in the $2S_{1/2}^{F=0}$ state are excited to the $4P_{1/2}^{F=1}$ ($4P_{3/2}^{F=1}$) state. The Lyman- γ (and, with lower efficiency, Lyman- α) extreme ultraviolet photons emitted by the atoms upon decay release photoelectrons from the graphite-coated inner walls of the detectors, which are subsequently counted by the detectors CEM1 and CEM2. The detector assembly is differentially pumped with a cryopump to ensure a background gas pressure lower than $1 \times 10^{-7} \text{ mbar}$ inside the 1S-2S and 2S-4P excitation regions.

The recorded counts are binned according to their arrival time τ into 10 delay time intervals $[\tau_i, \tau_{i+1}]$, ranging from delay times of 10 μs to 2621 μs . The width of the intervals was chosen in a way that provides comparable counting statistics to all 10 data sets and ranges from 50 μs for early delay times to 1711 μs for the longest delay time. The individual subsets of data obtained in this way sample different velocity groups of the excited atoms, which is used to constrain the first-order Doppler shift (see Sec. 2.1).

For each measurement setting, i.e. orientation of the linear laser polarization θ_L , the angle α between the spectroscopy laser beams and the atomic beam is adjusted to be close to $\alpha = 90^\circ$ before the actual data acquisition. This is achieved by blocking the spectroscopy laser beam before the HR mirror that otherwise retroreflects it and then minimizing the slope of the resulting first-order Doppler shift as a function of atomic velocity (36). Absolute frequency data

for the 2S-4P transitions is subsequently acquired with active Doppler compensation, i.e. with counter-propagating, actively stabilized (HR mirror tip/tilt) laser beams, for a specific setting of the laser polarization angle θ_L .

A single resonance scan consists of 29 randomized frequency points and takes about 90 s (35). The resonance is scanned by alternating between the red- and blue-detuned sides to reduce a possible bias in the deduced line centers by slow drifts in the fluorescence count rate caused by a drift in the number of 2S atoms reaching the 2S-4P excitation region. At each frequency point, the signal is integrated over 170 cycles of the chopper wheel, then the polarization is rotated by 90° (36) and the signal is integrated over another 170 cycles. This rotation of polarization is accomplished by coupling light from two paths into the two orthogonal polarization-maintaining axes of the fiber used for light delivery and successively switching between the paths. Typical resonances recorded with CEM2 for the first delay interval are shown in Fig. 2B in the main text.

For each measurement day, data are taken for a fixed value of θ_L and $\theta_L + 90^\circ$. In total, a typical measurement day consists of about 100 resonance scans per polarization direction, leading to a total number of about 4000 individual resonances per day (2 detectors, 2 polarization directions, 10 individual velocity subsets).

We observe background counts, i.e. counts when the spectroscopy laser is tuned off-resonance, caused by the decay of some of the metastable 2S atoms inside the detection region (the dark count rate of the detectors when no 2S atoms are present is negligible). The off-resonance background y_0 , measured relative to the on-resonance amplitude A above the background, is not identical for the two detectors. On average, $y_0/A \approx 0.21$ for CEM1 and $y_0/A \approx 0.10$ for CEM2, even though the amplitude A is very similar for CEM1 and CEM2. This background is much larger than the minimum background expected from the decay of unperturbed 2S atoms flying through the detector, which we estimate contributes only $y_0/A \approx 0.002$ and is expected to be identical for both detectors. We attribute the increased background to secondary electron emission from 2S atoms striking the downstream detector wall near CEM1. This is because the small size of the opening in the detector wall, designed to allow efficient differential pumping and a large detection solid angle, does not allow all 2S atoms to leave the detection region, especially in the presence of unavoidable small misalignments. This process can also account for the different background levels of the two detectors, since the detection efficiency of the secondary electrons emitted from the downstream detector wall is not expected to be identical between the detectors. We have also considered the possibility of collisional quenching, by a background gas, or Stark quenching, by stray electric fields, of the 2S atoms. We estimate the pressure of H₂ molecules, the dominant background gas in the vacuum chamber, needed to account for the observed background to be 9×10^{-6} mbar, by far exceeding the experimental upper limit on the pressure inside the detector, 1×10^{-7} mbar. Similarly, an electric field of 50 V/m would be needed for Stark quenching to explain the background, much larger than the experimental limit of 0.6 V/m (see Sec. 2.7).

Even though the background seen by the two detectors is different by more than a factor of two, the transition frequencies determined using our full analysis, but only the data from either

detector, are in excellent agreement. Using our numerical simulations, we have confirmed that the presence of a background due to the decay of 2S atoms does not influence the determined transition frequency. Additionally, we have also repeated the data analysis detailed below, but including a linear dependence of the background on laser detuning, and find the result to be in agreement with the result of the main analysis, which assumes only a constant background.

1.2 Line shape model

The line shape of an atom at rest which is subject to small distortions caused by quantum interference of one additional far-detuned resonance may be expressed by (28):

$$P(\omega, \vec{r}) \approx \frac{C}{(\omega - \omega_0)^2 + (\Gamma/2)^2} + a(\omega - \omega_0) + \frac{b(\omega - \omega_0)}{(\omega - \omega_0)^2 + (\Gamma/2)^2}, \quad (\text{S1})$$

where ω_0 is the frequency of the resonance of interest and Γ the natural line width of this resonance. The geometry dependence expressed by \vec{r} and the frequency separation Δ of the perturbing resonance from the resonance of interest is buried in the coefficients C, a, b . We drop the a term, as discussed in the main text, because the corresponding shifts are smaller than the shifts due to the b term by an additional factor of $\Gamma^2/\Delta^2 < 10^{-4}$ for the case of our 2S-4P spectroscopy, yielding

$$P(\omega, \vec{r}) \approx \frac{C}{(\omega - \omega_0)^2 + (\Gamma/2)^2} + \frac{b(\omega - \omega_0)}{(\omega - \omega_0)^2 + (\Gamma/2)^2}. \quad (\text{S2})$$

To take into account the finite Doppler width caused by the transverse divergence of the atomic beam, we convolve this line shape with a Gaussian:

$$p(\Delta\omega) = \frac{2\sqrt{\ln 2}}{\sqrt{\pi}\Gamma_G} e^{-4\ln 2 \frac{(\Delta\omega)^2}{\Gamma_G^2}}, \quad (\text{S3})$$

where Γ_G gives the FWHM of $p(\Delta\omega)$ that describes the probability to find an atom with its resonance frequency shifted by $\Delta\omega$ by the first-order Doppler shift. Γ_G can in principle be taken from the simulations of the atomic beam described in the discussion of the first-order Doppler shift, however there is a slight dependence on experimental parameters such as the angle between the atomic and laser beam. Since saturation effects and the resulting power-broadening of the resonance are not explicitly included in the line shape model, they will implicitly show up as an increase of both Γ_G and Γ over the value expected just from atomic beam divergence. Note that for short delay times ($\tau < 400 \mu\text{s}$), Doppler-broadening dominates, while for longer delay times saturation effects are the dominant broadening mechanism. For these reasons, both Γ_G and Γ are used as free parameters when fitting the experimental data. We find that Γ_G (Γ) ranges from 14 MHz (13 MHz) to 6 MHz (16 MHz) for the different delay times (see Sec. 2.1), leading to total FWHM line width ranging between 22 MHz and 17 MHz.

The convolution of Eq. S2 and Eq. S3 can be written as:

$$F(\omega) = C \frac{4\sqrt{\pi \ln 2}}{\Gamma_G \Gamma} \left\{ \text{Re}[w(z)] + \frac{\Gamma}{2C} \text{Im}[w(z)] \right\}, \quad (\text{S4})$$

with $z = 2\sqrt{\ln 2}[(\omega - \omega_0) + i\Gamma/2]/\Gamma_G$ and the Faddeeva function $w(z)$ given by (49)

$$w(z) \equiv e^{-z^2} \left(1 + \frac{2i}{\sqrt{\pi}} \int_0^z e^{t^2} dt \right). \quad (\text{S5})$$

Defining the asymmetry parameter as $\eta \equiv b\Gamma/4C$ and replacing the constant multiplicative prefactor with the free fit parameter $A = C \frac{4\sqrt{\pi \ln 2}}{\Gamma_G \Gamma}$, we recover the Fano-Voigt line shape given in Eq. 5 of the main text. To account for the experimental background (see Sec. 1.1), a constant term y_0 is added to the line shape (to Eq. S2 and thus Eq. S4) as a free fit parameter.

We test the Fano-Voigt line shape by fitting it to the results of the OBE simulation described in the main text and find a high suppression of quantum interference line shifts. To test the robustness of the fit and to control possible biases, we conduct a Monte Carlo simulation with the experimental frequency sampling of the resonance and the observed signal-to-noise ratio, including slow drifts in the latter, applied to the line shape from the OBE simulation.

1.3 Data analysis

Each recorded resonance, consisting of N pairs of laser frequency and number of fluorescence photons detected, is fit with the Fano-Voigt line shape with six free parameters (line center $\nu_0 = \omega_0/2\pi$, amplitude A , background y_0 , Lorentzian line width Γ , Gaussian line width Γ_G and asymmetry parameter η). We assume that the uncertainty $\sigma_{y,i}$ on the number of fluorescence photons detected y_i for each frequency point i is dominated by shot noise, i.e. $\sigma_{y,i} \approx \sqrt{y_i}$ (since $y_i \gg 1$, we can approximate the Poisson distribution with a normal distribution). The optimal values of the free parameters are then found by minimizing χ^2 , with the uncertainty of the values corresponding to an increase of χ^2 of 1 around the optimal values.

We use $\chi_{\text{red}}^2 = \chi^2/N_{\text{DOF}}$, with $N_{\text{DOF}} = N - 6$, as a measure of the goodness of fit. The resulting χ_{red}^2 distribution for the individual resonance fits deviates from the distribution expected for the assumed noise in two regards. First, the mode of the observed distribution is about 20% larger than expected, corresponding to a mean χ_{red}^2 of ~ 1.20 . Second, while the distribution follows the expected shape for $\chi_{\text{red}}^2 \lesssim 2$, there is an excess of resonance fits with $\chi_{\text{red}}^2 \gtrsim 2$.

The former is partly caused by the fact that while the Fano-Voigt line shape describes the observed line shape very well, there are small deviations between the two. The deviations can be decomposed in a contribution symmetric about the line center (up to 4% relative deviation) and a contribution asymmetric about the line center, more than an order of magnitude smaller than the symmetric contribution. The symmetric contribution is caused by (1) saturation effects related to the depletion of the initial $2S_{1/2}^{F=0}$ state and (2) non-Gaussian Doppler-broadening, both not included in the Fano-Voigt line shape. This symmetric contribution can lead to a sampling

bias, as discussed in Sec. 2.5. The asymmetric contribution is caused by quantum interference effects not described by the Fano-Voigt line shape and discussed in Sec. 2.4. These deviations increase the fit residuals over what would be expected from pure shot noise and shift the mode of the observed χ^2_{red} distribution to higher values. From our Monte Carlo simulation used to test the Fano-Voigt line shape (see Sec. 1.2), we expect this effect to increase the mode by 10%.

Additionally, there are other sources of noise present in the system. Besides shot noise, we expect the dominant noise contribution to be drifts in the number of 2S atoms reaching the 2S-4P excitation region caused by built-up of hydrogen ice on the cryogenic nozzle and drifts in the 243 nm laser power and in the condition of the RF discharge producing the hydrogen atoms. This additional noise also shifts the mode of the observed χ^2_{red} distribution to a higher value than expected for pure shot noise.

These drifts also cause an excess of resonance fits with $\chi^2_{\text{red}} \gtrsim 2$ as compared to the shot noise only situation, as can be deduced from our Monte Carlo simulation when properly modeling the drifts by interpolating the observed line amplitude and background as function of time. Another contribution are short (i.e. only affecting one or two frequency points), but large perturbations of the system, such as discharges in the detectors causing a short spike in count rate. To remove such events from the data analysis, a χ^2_{red} cut-off of 3 is introduced, i.e. individual resonance fits with a $\chi^2_{\text{red}} \geq 3$ are neglected in the data analysis. This results in a removal of less than 4% of the recorded resonances. The effect of this cut-off on the determined transition frequencies is within the final uncertainties.

By design, the free parameter η of the Fano-Voigt line shape is correlated with the line center ν_0 . For the typical signal-to-noise ratios of the recorded resonances, this leads to a significantly larger uncertainty on the line center when fitting the Fano-Voigt line shape as compared to fitting the Voigt line shape (where $\eta = 0$). To decrease this uncertainty, η is not treated as a free parameter for each resonance, but rather treated as one free parameter shared by a subset of resonances, effectively increasing the signal-to-noise ratio. Each subset only contains data taken for a specific laser polarization setting θ_L and for a single delay time interval and detector and thus subject to the same line distortions due to quantum interference corresponding to the same value of η . With this procedure, the uncertainty on the line center is reduced by about a factor of 2 and to the same level as when using the Voigt line shape. Since the Fano-Voigt line shape tends to be a numerically unstable fit for resonances where the Gaussian broadening is negligible ($\Gamma_G < 0.1$ MHz), we use a Fano-Lorentzian fit, i.e. the line shape given in Eq. S2 that does not include the Gaussian broadening of the Fano-Voigt. Both procedures, fitting using a shared η and using the Fano-Lorentzian fit where appropriate, do not change the determined transition frequencies within the fit uncertainty.

Finally, to determine the transition frequencies given in the main text, small model, sampling bias and light force shift corrections (see Sec. 2.4, 2.5 and 2.3) are determined for each recorded resonance and applied to the extracted line center. The transition frequencies are deduced by a weighted average of the line centers for all laser polarization settings θ_L , all delay times and both detectors, using the fit uncertainty on the line center as weight. The statistical uncertainty given corresponds to the uncertainty of the weighted average. The χ^2_{red} of this weighted average

is 1.16 for both the $2S-4P_{1/2}$ and $2S-4P_{3/2}$ transitions.

2 Corrections and uncertainties

Lists of the corrections applied and the contributions (at the one standard deviation σ level) to the total measurement uncertainty for two measured transitions $2S-4P_{1/2}$ and $2S-4P_{3/2}$ are given in table S2. We assume that the individual uncertainty contributions in each list are not correlated and add them in quadrature. The uncertainty contributions are, however, correlated between the two transition frequencies and we give the corresponding correlation coefficient r ($r_{X,Y} = \frac{\text{cov}(X,Y)}{\sigma_X \sigma_Y}$ for the contributions X, Y , with $\text{cov}(X, Y)$ the covariance between X and Y). The derived corrections and uncertainties for the 4P fine structure centroid ν_{2S-4P} and 4P fine structure splitting $\Delta\nu_{\text{FS}}^{\text{exp}}(4P)$ are given in Table 1 in the main text and table S3, respectively. In the following, each of the items in the lists is briefly discussed.

2.1 First-order Doppler shift

The suppression of the first-order Doppler shift using an active fiber-based retroreflector (AFR) and the experimental constraint on this suppression have been discussed in the main text and at length in (36). In contrast to (36), where a symmetric line shape was used to determine the line center, we here analyze our data as detailed in Sec. 1.3 using the Fano-Voigt line shape and small corrections from simulations. This is important because there is a dependence of the line distortions due to quantum interference on the interaction time with the spectroscopy beam and thus the mean velocity of the atoms (see Sec. 2.4). If those line distortions are not properly accounted for, they can result in an apparent shift of the transition frequency as a function of delay time, thus mimicking a Doppler shift.

The velocity distribution of the atoms for the different detection delay times is not only given by the initial velocity distribution of the atoms leaving the nozzle and the subsequent collimation by the apertures (see Fig. 3 of the main text), but is also influenced by the beam radius, power and detuning of the 243 nm laser that excites the ground state atoms to the $2S_{1/2}^{F=0}$ level. To model this, we perform a Monte Carlo simulation of atomic trajectories, taking into account the 1S-2S and 2S-4P excitation. To estimate the uncertainty of this approach, we vary the input parameters, including the initial velocity distribution, and compare the simulation results with experimentally accessible parameters such as the signal amplitude and line width for different delay times, which are both highly sensitive to the velocity distribution. The mean velocity v_i of atoms excited to the 4P level is found to range between 295(40) m/s and 85(10) m/s for the ten different delay time intervals, leading to an overall mean velocity of $\bar{v} = 240(30)$ m/s for all delay times considered. The transverse velocity distribution, i.e. along the direction of the 486 nm beams and relevant for Doppler broadening as opposed to a shift, is approximately Gaussian with a FWHM that ranges from 6(1) m/s down to 1.9(2) m/s.

Using these mean velocities v_i and the measured transition frequencies ν_i for the ten different delay time intervals, the rate of change m of the transition frequency as a function of mean velocity, or Doppler slope, can be extracted for different subsets of the data. This is done by fitting a linear model $\nu = mv + \delta\nu$ to the data, with the uncertainty on the Doppler slope derived from the uncertainty on the measured transition frequencies. If $\chi_{\text{red}}^2 = \chi^2/8$ of the determination is found to be above 1, the Doppler slope uncertainty is scaled with $\sqrt{\chi_{\text{red}}^2}$ to arrive at a conservative estimate of the Doppler slope uncertainty σ_m . Finally, the corresponding Doppler uncertainty $\sigma_{\nu,\text{D}}$ on the transition frequency averaged over the delay times is found by multiplying the Doppler slope uncertainty with overall mean velocity of all delay times, $\sigma_{\nu,\text{D}} = \sigma_m \bar{v}$.

When comparing the Doppler slopes extracted in this way for different measurement days, we find some excessive day-to-day scatter. We attribute this to slight misalignments in the AFR, such as in the angle α between the spectroscopy laser beams and the atomic beam or in the position of the beam waist of the laser beams, which should ideally coincide with HR mirror surface (36). Indeed, for a few measurement days the observed line width was slightly larger than on average, hinting at a possible slight misalignment of α . These misalignments can cause a residual Doppler shift with a sign depending on the direction of misalignment. Since the AFR is re-adjusted for most measurement days and since we expect the misalignments to be in a random direction, we expect the Doppler shift to compatible with zero when averaging over a sufficient number of days or, equivalently, re-alignments.

For the complete data set for each transition measured, we find the Doppler slopes to be $m = 0.7(12.1)$ Hz/(m/s) and $m = 9.5(11.8)$ Hz/(m/s) for the $2S-4P_{1/2}$ and $2S-4P_{3/2}$ transitions, respectively, and thus compatible with zero. The excessive scatter manifests itself in an increased χ_{red}^2 of 1.83 and 1.47 for the two transition and has already been taken into account for the uncertainties by scaling with $\sqrt{\chi_{\text{red}}^2}$. Since the Doppler slopes are found to be compatible with zero, we do not apply a correction to the transition frequencies, but only include the uncertainty on the slopes. Finally, the Doppler uncertainty on the transition frequencies $\nu_{1/2}$ and $\nu_{3/2}$ is found to be 2.92 kHz and 2.84 kHz, respectively. We assume the uncertainties to be uncorrelated for the two transitions ($r = 0$) and thus find a Doppler uncertainty of 2.13 kHz for ν_{2S-4P} .

2.2 Quantum interference

While we have thoroughly tested the compensation of line shifts due to quantum interference with the Fano-Voigt line shape using our simulations (see Sec. 1.2, 1.3 and 2.4), we here estimate the level of compensation directly from the experimental data. The basic idea is that any residual line shifts should follow the same functional behavior $\Delta\nu \equiv \Delta\nu(\theta_L)$, where θ_L is again the linear laser polarization angle, as the uncompensated line shifts seen when using the Voigt line shape for data analysis (see Fig. 4 (A and B) in the main text). For this purpose, we parametrize $\Delta\nu(\theta_L)$, starting from the analytical expression derived in the perturbative limit. For the $2S-4P_{1/2}$ transition, $\Delta\nu(\theta_L)$ is a simple sinusoidal function, while for the $2S-4P_{3/2}$ transition $\Delta\nu(\theta_L)$ is a more complicated function that can be approximated by a power series

in sinusoidal functions (as will be detailed elsewhere). The parametrization $\Delta\nu(\theta_L, A_{\text{res}}, \Delta\nu_0)$ has two free parameters, amplitude A_{res} and offset $\Delta\nu_0$, while the phase and period are fixed to the value of the uncompensated line shift and 180° , respectively. $\Delta\nu(\theta_L, A_{\text{res}}, \Delta\nu_0)$ is then fit to the data analyzed with the Fano-Voigt line shape, taking into account only the statistical uncertainty.

We first analyze the difference between the detectors, i.e. the difference in the observed line centers, which is somewhat more sensitive to quantum interference effects than the signal from the individual detectors. Here, we find a residual amplitude of $A_{\text{res}} = 4.46(1.36)$ kHz (compared to $54.8(1.3)$ kHz for the Voigt line shape) for the $2S-4P_{1/2}$ transition and a residual amplitude of $A_{\text{res}} = -1.68(2.00)$ kHz (compared to $28.6(2.0)$ kHz for the Voigt line shape) for the $2S-4P_{3/2}$ transition. Thus, the residual amplitude of the $2S-4P_{3/2}$ transition is compatible with zero, while there is small residual effect for $2S-4P_{1/2}$ transition.

To identify the origin of the residual amplitudes and to estimate the related uncertainty, we analyze the data of the individual detectors (see Fig. 4 (C and D) in the main text). The amplitudes of residual line shifts A_{res} are found to be well compatible with zero for detector CEM2 for the $2S-4P_{1/2}$ transition ($A_{\text{res}} = -0.09(0.84)$ kHz) and for both detectors CEM1 and CEM2 for the $2S-4P_{3/2}$ transition ($A_{\text{res}} = -0.16(1.23)$ kHz and $A_{\text{res}} = 0.11(1.06)$ kHz, respectively). For detector CEM1 and the $2S-4P_{1/2}$ transition, we find a small residual amplitude of $A_{\text{res}} = 3.23(1.16)$ kHz with a goodness of fit of $\chi^2_{\text{red}} = 6.6$. Thus, the residual amplitude seen in the difference is solely caused by the data from one of the detectors, CEM1. We note that otherwise the data from the two detectors, including the line shifts due to quantum interference (see Fig. 4 (A and B) in the main text), are very similar. To cross-check the compensation of asymmetries with the Fano-Voigt line shape, we have also analyzed the residual amplitudes using the Voigt line shape combined with our simulations (resulting in large corrections of tens of kilohertz) and find very similar results. The significance of this nonzero residual amplitude should be contrasted with the fact that a simple weighted average describes the data equally well ($\chi^2_{\text{red}} = 6.7$). Furthermore, as evident in the large χ^2_{red} , we have so far neglected residual Doppler shifts, which contribute an uncertainty as large as the residual amplitude and are expected to cause the day-to-day scatter seen here (with data for different θ_L values recorded on different days) (see Sec. 2.1). Note that discarding the data for $\theta_L = 0^\circ$ and $\theta_L = 90^\circ$ for the $2S-4P_{1/2}$ transition, which shows increased scatter as discussed in the main text, reduces the significance of the nonzero residual amplitude only slightly.

The transition frequencies given in the main text are determined by averaging over θ_L . To estimate residual quantum interference line shifts of these transition frequencies, the relation of the amplitude A_{res} and offset $\Delta\nu_0$ is investigated using our OBE simulations, using the experimental sampling of θ_L . We find $\Delta\nu_0/A_{\text{res}} \approx 0.2$ and $\Delta\nu_0/A_{\text{res}} \approx -0.2$ for the $2S-4P_{1/2}$ and $2S-4F_{3/2}$ transitions. With this, and after averaging over the two detectors, the residual line shifts are determined to be $0.29(33)$ kHz and $0.00(26)$ kHz for the $2S-4P_{1/2}$ and $2S-4P_{3/2}$ transitions, respectively, where $\chi^2_{\text{red}} > 1$ has been taken into account by scaling the uncertainties with $\sqrt{\chi^2_{\text{red}}}$.

We have tried to reproduce, using our simulations, the occurrence of a residual amplitude

in only one of the two detectors, but were not able to come up with a satisfactory explanation. One potential reason for a broken symmetry between the detectors is that the 2S-4P excitation region is not pointlike, but corresponds to the laser beam size (beam waist $w_0 = 1.85$ mm, detector radius 28 mm). This in turn leads to the two detectors observing slightly different solid angles and atomic velocities, and we indeed observe a slight differential Doppler shift between the two detectors.

However, when averaging over the two detectors and θ_L , both the line shifts due to this residual amplitude, as shown above, and the residual Doppler shift (see Sec. 2.1) are found to be compatible with zero, which is why we are confident that this residual effect does not influence our final results obtained by this average.

Thus, we assign an uncertainty of 0.33 kHz and 0.26 kHz due to residual quantum interference line shifts to the measured transition frequencies $\nu_{1/2}$ and $\nu_{3/2}$ respectively. Since the uncertainties are assumed to be limited by statistics, they are uncorrelated ($r = 0$) for the two transitions, resulting in an uncertainty of 0.20 kHz for $\nu_{\text{2S-4P}}$.

2.3 Light force shift

Atoms that are on a classical trajectory through a near-resonant standing wave may be subject to forces that are attractive to the nodes or anti-nodes for red or blue detuning, respectively (50). In this simple classical view, it seems obvious that the observed resonance can be distorted because this effect can enhance the red wing of the resonance while reducing the signal on the blue side, or, depending on the trajectory, vice versa. In fact one may model these line distortions by solving the OBEs with a position-dependent Rabi frequency simultaneously with Newton's equation of motion (51, 52). However, this simple classical description of atomic motion is attached to several conditions (52). One of them is that the atoms need to be sufficiently localized in order to assign a position-dependent force to them. In our case this condition is violated for two reasons: the transverse temperature of the 2S atoms is low enough to yield a coherence length of the atomic matter wave comparable to the periodicity of the optical potential ($\lambda/2 = 243$ nm). In addition, a single photon recoil is enough to separate the ground state part of the wave function by several half wavelengths from the excited state part while the atom crosses the 2S-4P spectroscopy beams.

The system then has to be described by including the atom's transverse momentum p along the 2S-4P spectroscopy laser beams in the quantum mechanical model together with the atom's internal dynamics. Interaction with the laser beams changes the atom's momentum by $\pm n\hbar k$, corresponding to the exchange of n photons with momentum $\hbar k$, and thus couples the corresponding momentum states, while spontaneous decay leads to a random recoil which averages to zero. In this picture, the coupling of the momentum states modifies the line shape of the transition probed and leads to a coherent superposition of the momentum states, corresponding to a partial localization similar to the classical picture. An analytic solution to this problem can be obtained with the effective Hamiltonian approach (see e.g. (53)), using the Wigner function to describe the initial momentum state of the atoms emerging from the nozzle and flying

through the apertures in the apparatus (subject of an upcoming publication). Because of the rapid decay of the 4P excited state to 1S ground state, the otherwise infinite momentum space can be reduced and $n = 4$ is found to be sufficient to describe the system. This analytic solution ignores the back decay of the excited 4P state to the initial $2S_{1/2}^{F=0}$ state, but since the branching ratio is only 4% this approximation is adequate and has been confirmed with more sophisticated models including this back decay. While it should in principle be possible to include effects that influence the initial momentum state such as the 1S-2S excitation in this analytical solution, we could also show that it is sufficient to describe the initial momentum state as a (fully delocalized) momentum eigenstate $|p\rangle$. We can then employ our OBE simulation to describe the system in a realistic experimental setting by including the momentum eigenstates $|p + n\hbar k\rangle$ along with the internal states of the atom. Using the atomic trajectories discussed in Sec. 2.1 as input for the OBE simulation, a Monte Carlo simulation can then be used to estimate shifts of the observed line center caused by the coupling of momentum states.

In this way, we find a light force shift of -0.43(40) kHz and -0.26(25) kHz for the $2S-4P_{1/2}$ and $2S-4P_{3/2}$ transitions, respectively. The $\nu_{1/2}$ and $\nu_{3/2}$ transition frequencies have been corrected for this shift. The uncertainty is limited by our knowledge of the atomic velocity distribution, which is correlated for the two transitions. Thus the uncertainties are fully correlated ($r = 1$) for the two transitions, leading to a correction of -0.32(30) kHz for ν_{2S-4P} .

2.4 Model corrections

The Fano-Voigt line shape is derived from the perturbative description of quantum interference, i.e. it does not account for effects such as back decay from the excited 4P state to the initial $2S_{1/2}^{F=0}$ state and the depletion of this initial state, leading to a saturation of the observed transition. In our system, 4% of the decays of the 4P state lead back to the initial $2S_{1/2}^{F=0}$ state and we excite about 30% of the 2S atoms to the 4P state. Under these conditions, the line asymmetries due to quantum interference can increase more than two-fold over the perturbative regime for the slowest probed atoms, i.e. those with longest interaction times with the spectroscopy laser. However, we find that the Fano-Voigt line shape is still a good description for our system, since the bulk of the increased line asymmetry is matched by it and thus can be accounted for by fitting the Fano-Voigt line shape to the observed resonances. Only a small residual asymmetry that does not match the asymmetry of the Fano-Voigt line shape remains. Importantly, this residual asymmetry is significantly less detection geometry-dependent than the asymmetry removed by the Fano-Voigt line shape, since it mainly stems from the small modification of the $2S_{1/2}^{F=0}$ population caused by the back decay of the 4P state to this state, which is independent of the detection geometry. This allows us to model this residual asymmetry without the need to accurately describe the detection geometry. The line shifts associated with this residual asymmetry depend on the intensity of and interaction time with the spectroscopy laser and are on the order of 1 kHz. As all effects stemming from quantum interference, the shifts are of opposite sign for the two perturbing resonances. Since the intensities in the experiment were chosen such that the Rabi frequencies are approximately identical for the two transitions probed, the shifts

are of ratio 2:1 for the $2S-4P_{1/2}$ and the $2S-4P_{3/2}$ transitions. Thus, for the 4P fine structure centroid ν_{2S-4P} they largely cancel.

Apart from these effects related to quantum interference, there is also an AC Stark shift of the atomic levels involved and a line shift associated with off-resonant excitations caused by optical pumping into the $2S_{1/2}^{F=1}$ states. Both contributions lead to small shifts of the observed line center on the order of 0.10 kHz. The initial population in the $2S_{1/2}^{F=1}$ states from Doppler-sensitive two-photon excitation is negligible compared to the population accumulated in these states through optical pumping.

All these effects are included in the OBE simulations of our system. For each recorded resonance, a corresponding line shape is generated from the OBE simulation. Experimental noise, consisting of shot noise and slow drifts in the number of 2S atoms contributing to the signal, is added and the resulting resonance is fit with the Fano-Voigt line shape, a process that is repeated multiple times in the fashion of a Monte Carlo simulation. The line center determined from these fits is then used a model correction for the recorded resonances. With this, we find a model correction of 1.34(23) kHz and -0.50(10) kHz for the $\nu_{1/2}$ and $\nu_{3/2}$ transition frequencies, respectively. The uncertainty is estimated by varying the input parameters to the OBE simulation within the experimental constraints. Some of the contributions to the uncertainty, such as the spectroscopy laser power, are uncorrelated, while others, such as the atomic velocity distribution, are correlated for the two transition measurements. The total uncertainty is found to be partially anticorrelated ($r = -0.65$) for the two measurements, resulting in a model correction of 0.11(6) kHz for ν_{2S-4P} .

2.5 Sampling bias

As has been detailed in Sec. 1.3, there are small deviations symmetric about the line center between the observed line shape and the Fano-Voigt line shape used for data analysis (the asymmetric deviations are much smaller and included in the model corrections discussed in Sec. 2.4). In combination with an experimental frequency sampling of the resonances that is not quite symmetric about the line center, this can lead to a bias in the line center determined from the fit to the resonance. We use our Monte Carlo simulations discussed in Sec. 2.4 to estimate this bias and find it to be up to 2.1 kHz for the $2S-4P_{3/2}$ transition.

To reduce this bias, we enforce fair sampling of the resonance by selectively removing up to two experimental frequency points for each resonance. The procedure is the following: First, the simulated resonance is fit with the Fano-Voigt line shape for all available simulation points and with no experimental noise added. Then, it is fit for the experimental frequency points, with the difference in extracted line centers giving the bias to be reduced. Next, experimental frequency points are removed and the simulated resonance is fit again. This is repeated for all combinations of removing one or two points. Finally, we choose to remove the one or two experimental points without which the bias is lowest (no point is removed if the bias is lowest for full sampling), resulting on the removal of 1.94 frequency points on average. This procedure is applied to every recorded resonance. The experimental data is then fit again with these points

removed, leading to a slight increase in the statistical uncertainty of approximately 4%.

After applying this procedure, the sampling bias is, again using the Monte Carlo simulations, found to be 0.34 kHz and 0.83 kHz for the 2S-4P_{1/2} and 2S-4P_{3/2} transitions, respectively. The transition frequencies $\nu_{1/2}$ and $\nu_{3/2}$ have been corrected for this bias and an uncertainty of 0.40 kHz and 0.70 kHz, respectively, is assigned to these corrections. This uncertainty accounts for the fact that a separate OBE simulation is used to estimate the light force shift (see Sec. 2.3) and that this simulation shows very similar symmetric deviations (since it also includes the same saturation effects and same Doppler-broadening as the quantum interference OBE simulation) and thus leads to a very similar sampling bias. In order to avoid a double counting of this bias, we only correct for the bias found for the quantum interference OBE simulation, but add the bias of the light force shift OBE simulation as uncertainty. The uncertainty for the two transitions is uncorrelated ($r = 0$), and thus ν_{2S-4P} includes a correction of 0.44(49) kHz.

2.6 Second-order Doppler shift

The second-order Doppler effect is not canceled by the excitation of the 2S-4P transition utilizing phase-retracing beams. However, the signal weighted, mean squared velocity $\overline{v^2} = 255(30)$ m/s provided by the cryogenic source of 2S atoms and estimated using the Monte Carlo simulations described above, is sufficiently small so that the second-order Doppler shift only amounts to

$$\Delta\nu_{\text{SOD}} = -\frac{1}{2} \frac{\overline{v^2}}{c^2} \nu_{2S-4P} = -0.22(5) \text{ kHz.} \quad (\text{S6})$$

The measured transitions frequencies $\nu_{1/2}$ and $\nu_{3/2}$ are corrected for the second-order Doppler shift by subtracting $\Delta\nu_{\text{SOD}}$. The uncertainty is fully correlated ($r = 1$) for the two transitions, and thus the correction and uncertainty for ν_{2S-4P} is the same as for the individual frequencies.

2.7 dc-Stark shift

Special care was taken to suppress stray electric fields in the 2S-4P excitation region to avoid the associated line shifts due to the dc-Stark effect. A grounded Faraday cage made from stainless steel mesh with two wires (diameter 30 µm) per millimeter shields the excitation region from the static electric fields created by the channel electron multiplier input surfaces (+270 V) (see Fig. 3 in the main text). The Faraday cage and all surfaces in the excitation region are spray-coated with colloidal graphite to suppress the built-up of patch charges and to avoid fields due to contact potentials. An upper limit of 0.6 V/m has been obtained for the field strength of stray electric fields using 1S-2S spectroscopy in a dedicated setup with similar dimensions and identical coating (1, 2, 54). We use this upper limit on the field strength to estimate line shifts for the 2S-4P transitions.

The dc-Stark effect shifts the energies of the 4P_{1/2}^{F=1} and 4P_{3/2}^{F=1} levels (the shift of the 2S_{1/2}^{F=0} level is negligible on the current level of accuracy) in the presence of a static electric field \vec{F} , with the energy shift $\Delta\omega = 2\pi \times a_{j,m_F} F^2$ proportional to the square of the field strength

$F = |\vec{F}|$. The coefficients a_{j,m_F} depends on the orientation of the static electric field \vec{F} with respect to the quantization axis of the atom, given by the linear laser polarization \vec{E} . The coefficients a_{j,m_F} , derived by diagonalizing the atomic Hamiltonian in the presence of a static electric field and fitting the resulting energy shifts with a quadratic function, are shown in table S1.

The upper limit for the dc-Stark shift of the transition frequencies for the worst case orientation of the stray electric fields is -0.03 kHz and -0.49 kHz for the $2S-4P_{1/2}$ and $2S-4P_{3/2}$ transitions, respectively. However, we assume that the orientation of possible stray electric fields \vec{F} is not correlated with the orientation of the linear polarization \vec{E} of the spectroscopy laser. Since the transition frequencies $\nu_{1/2}$ and $\nu_{3/2}$ are determined from data taken for different orientations of the laser polarization (see Fig. 4 in the main text), the upper limit on the dc-Stark shift for these transitions is further reduced by averaging over the different orientations of stray electric fields. With this, we estimate an uncertainty due to the dc-Stark shift of 0.03 kHz and 0.30 kHz for the $\nu_{1/2}$ and $\nu_{3/2}$ transition frequencies, respectively. The uncertainty for the two transitions is uncorrelated ($r = 0$) and the combined uncertainty is 0.20 kHz for ν_{2S-4P} .

Furthermore, we note that the shift of the line center extracted by fitting the observed resonance may be smaller than the shift of the energy levels, since the electric field does not only shift the energy of the involved levels, but mixes different atomic levels. In this way, excitations of the $4S$ and $4D$ levels (which now have some admixture of the $4P$ level) become dipole-allowed. These transitions tend to cancel out the dc-Stark shift of the $4P$ levels when the transitions are within the recorded laser frequency range. We have however not fully investigated this cancellation, which depends on the excitation dynamics of the system, and thus here use the shift of the energy levels as upper limit for the shift of the resonances.

2.8 Zeeman shift

The earth's magnetic field is pre-compensated by three orthogonal pairs of Helmholtz coils outside the vacuum chamber. In addition, the $2S-4P$ excitation region is shielded from residual magnetic fields by a double-layer high-permeability metal (mu-metal) shield. Thereby, magnetic fields are suppressed to less than 1 mG in a volume of about 15 cm 3 around the $2S-4P$ excitation region.

For a given magnetic flux density B , the linear Zeeman effect shifts the energies of the magnetic sublevels $m_F = \pm 1$ of the $4P_{1/2}^{F=1}$ ($4P_{3/2}^{F=1}$) state by $\Delta E/\hbar = g_F \mu_B B m_F / \hbar = 2\pi \times 0.467$ kHz/mG ($\Delta E/\hbar = 2\pi \times 2.33$ kHz/mG), using the appropriate g-factor g_F and the Bohr magneton μ_B . The observed transition frequency, i.e. the center of weight of the signals from the different magnetic sublevels, will only be shifted if the $m_F = \pm 1$ sublevels contribute with different amplitudes. This situation requires some circularly polarized light about the direction of the magnetic field, i.e. a mismatch in the intensities $|E_L|^2$ and $|E_R|^2$ of the left- and right-polarized components as given by the Stokes parameter $v = (|E_L|^2 - |E_R|^2) / (|E_L|^2 + |E_R|^2)$. An upper limit for the shift of the observed transition frequency of $\Delta\omega = \Delta E/\hbar \times v$ is obtained by assuming that the magnetic field is aligned along the spectroscopy laser beam.

We determine v from the measured intensity polarization extinction ratio $P_{\text{er}} = 1/200$, limited by the polarization-maintaining fiber, and find $v = 0.14$. Thus, we estimate the uncertainty due to the Zeeman shift to be below 0.07 kHz and 0.33 kHz for the $\nu_{1/2}$ and $\nu_{3/2}$ transition frequencies, respectively. The shift is uncorrelated ($r = 0$) for the two measured transitions and a combined uncertainty of 0.22 kHz is assigned for ν_{2S-4P} . The quadratic Zeeman effect that would also affect the initial $2S_{1/2}^{F=0}, m_F = 0$ and the $4P_{1/2}^{F=1}, m_F = 0$ and $4P_{3/2}^{F=1}, m_F = 0$ states is negligible at our current level of accuracy.

2.9 Pressure shift

To estimate the pressure shift we use the impact approximation for binary collisions (55). The interaction energy between the perturbed and the perturbing atom is required as input for this theory and is given by the near-field dipole-dipole interaction:

$$\hat{V} = \frac{1}{4\pi\varepsilon_0 R^3} \left(\hat{d}_{1x}\hat{d}_{2x} + \hat{d}_{1y}\hat{d}_{2y} - 2\hat{d}_{1z}\hat{d}_{2z} \right), \quad (\text{S7})$$

where R is the distance between the atoms and \hat{d}_{ij} with $j = x, y, z$ are the components of the electric dipole moment for the perturbing ($i = 1$) and perturbed ($i = 2$) atoms. The energy shift of the product state $|n\rangle = |n_1\rangle \otimes |n_2\rangle = |n_1, n_2\rangle$ of the perturbing and perturbed atoms due to the Van-der-Waals interaction can be calculated using second-order perturbation theory:

$$E_{\text{vdW}}(n) = \sum_{m, E_n \neq E_m} \frac{|\langle n | \hat{V} | m \rangle|^2}{E_n - E_m} = \frac{C_6}{R^6}, \quad (\text{S8})$$

where $|m\rangle$ are all possible product states of the two atoms and E_m is the energy of state $|m\rangle$. The interaction energy is thus $\propto 1/R^6$ and the strength of the interaction is expressed by the coefficient C_6 . For resonant interactions, $E_n - E_m = 0$, and Eq. S8 is not valid anymore. Furthermore, in our case the perturbing and perturbed atoms can be connected by dipole-allowed transition (e.g. colliding 4P and 1S atoms) and thus a resonant interaction of $|n_1, n_2\rangle$ with $|n_2, n_1\rangle$ and non-vanishing $\langle n_1, n_2 | \hat{V} | n_2, n_1 \rangle$ is possible, corresponding to an excitation exchange between the atoms. Nevertheless, it is well known that these interactions only cause a line broadening, but do not cause a line shift (56). Hence we can estimate the largest contribution with the smallest possible $E_n - E_m$ and use the analytic expressions for the dipole matrix elements for colliding hydrogen atoms in any states. Furthermore, we assume that all perturbing particles are 1S atoms, since the density of 2S atoms is only $\sim 10^{-3}$ of the 1S atom density and the contribution due to collisions with background molecules can be neglected as there is no close degeneracy. The perturbation of atoms in the 2S initial state causes a negligible line shifts on the current level of accuracy, leaving only the perturbation of the excited $4P_j$ atoms caused by collisions with 1S atoms to consider. We approximate the sum in Eq. S8 with the minimum combined internal energy difference given by the hyperfine splitting of $4P_j$ states (7.39623(7) MHz for $j = 1/2$ and 2.95647(3) MHz for $j = 3/2$, see Fig. 2A in the main text) and obtain

$$C_6(4P_{1/2} - 1S) = 1.9 \times 10^5 hcR_\infty a_0^6, \quad C_6(4P_{3/2} - 1S) = 1.9 \times 10^6 hcR_\infty a_0^6, \quad (\text{S9})$$

with the Bohr radius a_0 . Within the impact approximation the C_6 Van-der-Waals interaction leads to a frequency shift of (55)

$$\Delta\omega \approx 2.9 \left(\frac{C_6}{\hbar} \right)^{2/5} v^{3/5} N, \quad (\text{S10})$$

where v is velocity of colliding atoms and N is the density of the perturbing atoms. From our experimental data, we estimate the concentration of $1S$ atoms in the beam to be $N_{\text{beam}} \approx 2.2 \times 10^{15}$ atoms/m³ at temperature 5 K and the concentration of background atoms to be not more than $N_{\text{bkg}} \approx 2.4 \times 10^{15}$ atoms/m³ at temperature 300 K. Estimating the collisional velocity of the atoms by their mean velocity, we find the contributions to the pressure shifts of the two measured transitions to be $\Delta\omega(4P_{1/2} - 1S, \text{beam-beam}) \approx 2\pi \times 3$ Hz, $\Delta\omega(4P_{1/2} - 1S, \text{beam-background}) \approx 2\pi \times 9$ Hz, $\Delta\omega(4P_{3/2} - 1S, \text{beam-beam}) \approx 2\pi \times 8$ Hz and $\Delta\omega(4P_{3/2} - 1S, \text{beam-background}) \approx 2\pi \times 23$ Hz. Thus, the pressure shift is estimated to be below 0.01 kHz for the $2S$ - $4P_{1/2}$ transition and below 0.03 kHz for the $2S$ - $4P_{3/2}$ transition. The uncertainty is assumed to be fully correlated ($r = 1$) for the two transitions, resulting in an uncertainty of 0.02 kHz for ν_{2S-4P} .

2.10 Laser spectrum and frequency calibration

The two laser systems used in the measurement, the spectroscopy laser for $2S$ - $4P$ excitation at 486 nm and the preparation laser for $1S$ - $2S$ excitation at 243 nm, share a similar design. Both laser systems consist of an external cavity diode laser as master oscillator running at 972 nm (57). The frequency of the lasers is stabilized to high-finesse Fabry-Pérot cavities (58), which reduces the laser line width to a few Hz. However, the delta-shaped laser line sits on a weak but broad noise pedestal (58). After power amplification with a tapered amplifier, the light is frequency doubled (frequency doubled twice) to 486 nm (243 nm) for the spectroscopy (excitation) laser system. The spectral purity of the lasers is routinely monitored by a beat note between the two systems at 486 nm.

Asymmetries of the noise pedestal that might fold into the observed $2S$ - $4P$ line shapes are small because of the use of long external cavity diode lasers (see (57, 58)). We obtain an upper limit of 0.10 kHz by artificially removing the noise pedestal on one side of the measured laser spectrum, numerically folding it into the $2S$ - $4P$ line shape, and fitting the result. The same laser was used for both transition measurements and thus the upper limit is fully correlated ($r = 1$) for the two measurements.

Both laser systems are phase-coherently linked to an Er-doped fiber frequency comb which is referenced to an active hydrogen maser. The maser serves as the frequency reference for the experiment and is calibrated (steered) via the global positioning system (GPS), resulting in a fractional frequency uncertainty of 1 part in 10^{13} . The maser calibration uncertainty translates to an uncertainty of 0.06 kHz for the $2S$ - $4P$ transition frequencies and is fully correlated ($r = 1$) for the two measured transitions.

The absolute frequencies of the laser systems are determined with a beat note with the frequency comb at 972 nm. The frequency of the 2S-4P spectroscopy light ν_{Laser}^{486} at 486 nm at a given time t can be deduced from the beat note data with

$$\nu_{\text{Laser}}^{486} = 2 \times (N \times \nu_{\text{rep}} + 2\nu_{\text{CEO}} - \nu_{\text{LO}}) + 2 \times (\nu_{\text{beat}}(t) - \nu_{\text{AOM}}(t)), \quad (\text{S11})$$

where $\nu_{\text{rep}} = 250$ MHz denotes the repetition rate of the frequency comb, $\nu_{\text{CEO}} = 30$ MHz the carrier-envelope offset frequency, ν_{LO} the frequency of an additional local oscillator used to mix down the frequency of the beat note to $\nu_{\text{beat}}(t) \approx 20$ MHz and $\nu_{\text{AOM}}(t) \approx 350 \pm 30$ MHz the frequency of the acousto-optic modulator (AOM) used for scanning over the atomic resonance. The comb mode numbers are $N = 1\,233\,042$ and $N = 1\,233\,044$ for the measurement of the 2S-4P_{1/2} and 2S-4P_{3/2} transitions, respectively.

The laser frequencies are determined with a linear fit of the comb beat note data $\nu_{\text{beat}}(t)$ and using Eq. S11, leading to an uncertainty in the laser frequency determination of less than 0.10 kHz for each recorded resonance. This leads to a negligible uncertainty for the determined transition frequencies.

2.11 Recoil shift

Energy and momentum conservation require the absorbed photon energy to be larger than the atomic resonance frequency ν by the recoil shift of the atom upon absorption. The corresponding recoil shift can be written as

$$\Delta\nu_{\text{recoil}} = \frac{h}{2M_{\text{H}}} \left(\frac{\nu}{c}\right)^2 \approx 837.23 \text{ kHz}, \quad (\text{S12})$$

with the mass of the hydrogen atom M_{H} . $\Delta\nu_{\text{recoil}}$ is known with much smaller uncertainty than required here. h/M_{H} can be calculated using the experimental values of the ratio h/m_e of the Planck constant h and the electron mass m_e , the binding energy of the H atom and the mass of the proton and the electron in atomic mass units (3). The transition frequencies $\nu_{1/2}$, $\nu_{3/2}$ and $\nu_{\text{2S-4P}}$ given in the main text have been corrected for the recoil shift.

2.12 Hyperfine corrections

In order to obtain the transition frequency from the 2S hyperfine centroid to the 4P fine structure centroid (see fig. S1), the measured transition frequencies $\nu_{1/2}$ and $\nu_{3/2}$ have to be corrected for the hyperfine shift of the 2S_{1/2}^{F=0}, 4P_{1/2}^{F=1} and 4P_{3/2}^{F=1} states (table II in (38))

$$\Delta\nu_{\text{HFS}}(2\text{S}_{1/2}^{F=0}) = -133\,167.6257(51) \text{ kHz}, \quad (\text{S13})$$

$$\Delta\nu_{\text{HFS}}(4\text{P}_{1/2}^{F=1}) = +1848.8(1) \text{ kHz}, \quad (\text{S14})$$

$$\Delta\nu_{\text{HFS}}(4\text{P}_{3/2}^{F=1}) = -1847.7(1) \text{ kHz}. \quad (\text{S15})$$

These shifts have been obtained experimentally (for 2S, see (59)) and by extrapolation to higher n and include a small off-diagonal term of $\Delta\nu_{\text{HFS}}^{\text{o.d.}} = \pm 0.313$ kHz for the 4P states. The transition frequency from the 2S hyperfine centroid to the 4P fine structure centroid, $\nu_{2\text{S}-4\text{P}}$ (Eq. 9 in the main text), is obtained by a weighted average of the hyperfine centroids

$$\begin{aligned}\nu_{2\text{S}-4\text{P}} &= \frac{1}{3} (\nu_{1/2} - \Delta\nu_{\text{HFS}}(4\text{P}_{1/2}^{F=1})) + \frac{2}{3} (\nu_{3/2} - \Delta\nu_{\text{HFS}}(4\text{P}_{3/2}^{F=1})) + \Delta\nu_{\text{HFS}}(2\text{S}_{1/2}^{F=0}) \\ &= \frac{1}{3}\nu_{1/2} + \frac{2}{3}\nu_{3/2} - 132\,552.092(75) \text{ kHz.}\end{aligned}\quad (\text{S16})$$

The fine structure splitting $\Delta\nu_{\text{FS}}^{\text{theo}}(4\text{P})$ of the $4\text{P}_{1/2}^{F=1}$ and $4\text{P}_{3/2}^{F=1}$ states may readily be obtained from the difference in the total binding energies of the $4\text{P}_{1/2}^{F=1}$ and $4\text{P}_{3/2}^{F=1}$ states given in table IV in (38)

$$\Delta\nu_{\text{FS}}^{\text{theo}}(4\text{P}) = 1\,367\,433.3(3) \text{ kHz.}\quad (\text{S17})$$

Supplementary figures

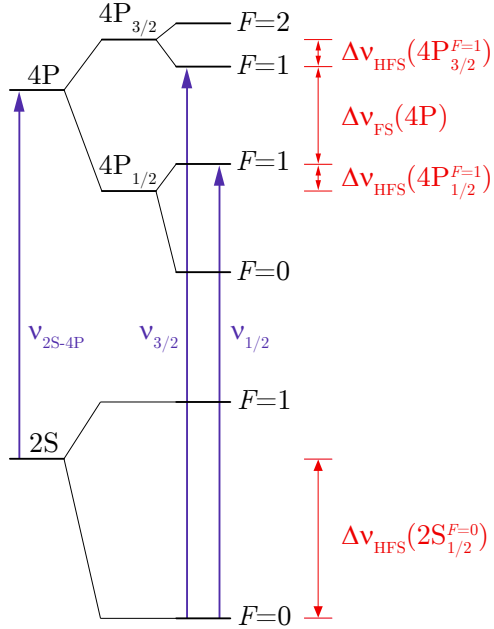


Figure S1: Hydrogen 2S-4P level scheme (not to scale). The transition frequencies of the $2S_{1/2}^{F=0}-4P_{1/2}^{F=1}$ ($\nu_{1/2}$) and $2S_{1/2}^{F=0}-4P_{3/2}^{F=1}$ ($\nu_{3/2}$) transition are experimentally determined. The transition frequency from the 2S hyperfine structure centroid to the 4P fine structure centroid, ν_{2S-4P} , is determined by combining $\nu_{1/2}$ and $\nu_{3/2}$ and correcting for the hyperfine shifts $\Delta\nu_{HFS}(2S_{1/2}^{F=0})$, $\Delta\nu_{HFS}(4P_{1/2}^{F=1})$ and $\Delta\nu_{HFS}(4P_{3/2}^{F=1})$. The fine structure splitting $\Delta\nu_{FS}(4P)$ corresponds to the energy difference of the $4P_{1/2}^{F=1}$ and $4P_{3/2}^{F=1}$ states.

Supplementary tables

Table S1: List of quadratic coefficients for the dc-Stark effect for the relevant atomic levels and different orientations of the static electric field \vec{F} with respect to the laser polarization \vec{E} .

Level	Orientation of \vec{F}	a_{j,m_F} (Hz/(V/m) ²)
$4P_{1/2}^{F=1}$	$\vec{F} \parallel \vec{E}$	-97
$4P_{1/2}^{F=1}$	$\vec{F} \perp \vec{E}$	-83
$4P_{3/2}^{F=1}$	$\vec{F} \parallel \vec{E}$	186
$4P_{3/2}^{F=1}$	$\vec{F} \perp \vec{E}$	-1354

Table S2: List of corrections $\Delta\nu$ and uncertainties σ for the determination of the $2S_{1/2}^{F=0}$ - $4P_{1/2}^{F=1}$ ($\nu_{1/2}$) and $2S_{1/2}^{F=0}$ - $4P_{3/2}^{F=1}$ ($\nu_{3/2}$) transition frequencies and the correlation coefficient r of the uncertainties for the two transitions.

Contribution	$2S_{1/2}^{F=0}$ - $4P_{1/2}^{F=1}$ ($\nu_{1/2}$)		$2S_{1/2}^{F=0}$ - $4P_{3/2}^{F=1}$ ($\nu_{3/2}$)		Correlation coefficient
	$\Delta\nu$ (kHz)	σ (kHz)	$\Delta\nu$ (kHz)	σ (kHz)	
Statistics	0.00	0.48	0.00	0.56	0
First-order Doppler shift	0.00	2.92	0.00	2.84	0
Quantum interference shift	0.00	0.33	0.00	0.26	0
Light force shift	-0.43	0.40	-0.26	0.25	1
Model corrections	1.34	0.23	-0.50	0.10	-0.65
Sampling bias	-0.34	0.40	0.83	0.70	0
Second-order Doppler shift	0.22	0.05	0.22	0.05	1
dc-Stark shift	0.00	0.03	0.00	0.30	0
Zeeman shift	0.00	0.07	0.00	0.33	0
Pressure shift	0.00	0.01	0.00	0.03	1
Laser spectrum	0.00	0.10	0.00	0.10	1
Frequency standard (hydrogen maser)	0.00	0.06	0.00	0.06	1
Recoil shift	-837.23	0.00	-837.23	0.00	n/a
Total	-836.4	3.0	-836.9	3.0	0.011

Table S3: List of corrections $\Delta\nu$ and uncertainties σ for the determination of the 4P fine structure splitting $\Delta\nu_{\text{FS}}^{\text{exp}}(4\text{P})$.

Contribution	$\Delta\nu$ (kHz)	σ (kHz)
Statistics	0.00	0.74
First-order Doppler shift	0.00	4.07
Quantum interference shift	0.00	0.42
Light force shift	0.17	0.15
Model corrections	-1.84	0.30
Sampling bias	1.17	0.81
Second-order Doppler shift	0.00	0.00
dc-Stark shift	0.00	0.30
Zeeman shift	0.00	0.34
Pressure shift	0.00	0.02
Laser spectrum	0.00	0.10
Frequency standard (hydrogen maser)	0.00	0.06
Recoil shift	0.00	0.00
Total	-0.5	4.3

References and Notes

1. C. G. Parthey, A. Matveev, J. Alnis, B. Bernhardt, A. Beyer, R. Holzwarth, A. Maistrou, R. Pohl, K. Predehl, T. Udem, T. Wilken, N. Kolachevsky, M. Abgrall, D. Rovera, C. Salomon, P. Laurent, T. W. Hänsch, Improved measurement of the hydrogen 1S-2S transition frequency. *Phys. Rev. Lett.* **107**, 203001 (2011).
[doi:10.1103/PhysRevLett.107.203001](https://doi.org/10.1103/PhysRevLett.107.203001) [Medline](#)
2. A. Matveev, C. G. Parthey, K. Predehl, J. Alnis, A. Beyer, R. Holzwarth, T. Udem, T. Wilken, N. Kolachevsky, M. Abgrall, D. Rovera, C. Salomon, P. Laurent, G. Grosche, O. Terra, T. Legero, H. Schnatz, S. Weyers, B. Altschul, T. W. Hänsch, Precision measurement of the hydrogen 1S-2S frequency via a 920-km fiber link. *Phys. Rev. Lett.* **110**, 230801 (2013).
[doi:10.1103/PhysRevLett.110.230801](https://doi.org/10.1103/PhysRevLett.110.230801) [Medline](#)
3. P. J. Mohr, D. B. Newell, B. N. Taylor, CODATA recommended values of the fundamental physical constants: 2014. *Rev. Mod. Phys.* **88**, 035009 (2016).
[doi:10.1103/RevModPhys.88.035009](https://doi.org/10.1103/RevModPhys.88.035009)
4. R. Pohl, A. Antognini, F. Nez, F. D. Amaro, F. Biraben, J. M. R. Cardoso, D. S. Covita, A. Dax, S. Dhawan, L. M. P. Fernandes, A. Giesen, T. Graf, T. W. Hänsch, P. Indelicato, L. Julien, C.-Y. Kao, P. Knowles, E.-O. Le Bigot, Y.-W. Liu, J. A. M. Lopes, L. Ludhova, C. M. B. Monteiro, F. Mulhauser, T. Nebel, P. Rabinowitz, J. M. F. Dos Santos, L. A. Schaller, K. Schuhmann, C. Schwob, D. Taqqu, J. F. C. A. Veloso, F. Kottmann, The size of the proton. *Nature* **466**, 213–216 (2010). [doi:10.1038/nature09250](https://doi.org/10.1038/nature09250) [Medline](#)
5. A. Antognini, F. Nez, K. Schuhmann, F. D. Amaro, F. Biraben, J. M. R. Cardoso, D. S. Covita, A. Dax, S. Dhawan, M. Diepold, L. M. P. Fernandes, A. Giesen, A. L. Gouvea, T. Graf, T. W. Hänsch, P. Indelicato, L. Julien, C.-Y. Kao, P. Knowles, F. Kottmann, E.-O. Le Bigot, Y.-W. Liu, J. A. M. Lopes, L. Ludhova, C. M. B. Monteiro, F. Mulhauser, T. Nebel, P. Rabinowitz, J. M. F. dos Santos, L. A. Schaller, C. Schwob, D. Taqqu, J. F. C. A. Veloso, J. Vogelsang, R. Pohl, Proton structure from the measurement of 2S-2P transition frequencies of muonic hydrogen. *Science* **339**, 417–420 (2013).
[doi:10.1126/science.1230016](https://doi.org/10.1126/science.1230016) [Medline](#)
6. R. Pohl, R. Gilman, G. A. Miller, K. Pachucki, Muonic hydrogen and the proton radius puzzle. *Annu. Rev. Nucl. Part. Sci.* **63**, 175–204 (2013).
[doi:10.1146/annurev-nucl-102212-170627](https://doi.org/10.1146/annurev-nucl-102212-170627)
7. J. C. Bernauer, R. Pohl, The proton radius problem. *Sci. Am.* **310**, 32–39 (2014).
[doi:10.1038/scientificamerican0214-32](https://doi.org/10.1038/scientificamerican0214-32) [Medline](#)
8. C. E. Carlson, The proton radius puzzle. *Prog. Part. Nucl. Phys.* **82**, 59–77 (2015).
[doi:10.1016/j.ppnp.2015.01.002](https://doi.org/10.1016/j.ppnp.2015.01.002)
9. J. C. Bernauer, P. Achenbach, C. Ayerbe Gayoso, R. Böhm, D. Bosnar, L. Debenjak, M. O. Distler, L. Doria, A. Esser, H. Fonvieille, J. M. Friedrich, J. Friedrich, M. Gómez Rodríguez de la Paz, M. Makek, H. Merkel, D. G. Middleton, U. Müller, L. Nungesser, J. Pochodzalla, M. Potokar, S. Sánchez Majos, B. S. Schlimme, S. Širca, T. Walcher, M. Weinriefer, A1 Collaboration, High-precision determination of the electric and magnetic

form factors of the proton. *Phys. Rev. Lett.* **105**, 242001 (2010).
[doi:10.1103/PhysRevLett.105.242001](https://doi.org/10.1103/PhysRevLett.105.242001) [Medline](#)

10. X. Zhan, K. Allada, D. S. Armstrong, J. Arrington, W. Bertozzi, W. Boeglin, J.-P. Chen, K. Chirapatpimol, S. Choi, E. Chudakov, E. Cisbani, P. Decowski, C. Dutta, S. Frullani, E. Fuchey, F. Garibaldi, S. Gilad, R. Gilman, J. Glister, K. Hafidi, B. Hahn, J.-O. Hansen, D. W. Higinbotham, T. Holmstrom, R. J. Holt, J. Huang, G. M. Huber, F. Itard, C. W. de Jager, X. Jiang, M. Johnson, J. Katich, R. de Leo, J. J. LeRose, R. Lindgren, E. Long, D. J. Margaziotis, S. May-Tal Beck, D. Meekins, R. Michaels, B. Moffit, B. E. Norum, M. Olson, E. Piasetzky, I. Pomerantz, D. Protopopescu, X. Qian, Y. Qiang, A. Rakhman, R. D. Ransome, P. E. Reimer, J. Reinhold, S. Riordan, G. Ron, A. Saha, A. J. Sarty, B. Sawatzky, E. C. Schulte, M. Shabestari, A. Shahinyan, R. Shneor, S. Širca, P. Solvignon, N. F. Sparveris, S. Strauch, R. Subedi, V. Sulcosky, I. Vilardi, Y. Wang, B. Wojtsekhowski, Z. Ye, Y. Zhang, High-precision measurement of the proton elastic form factor ratio $\mu_p G_E/G_M$ at low Q^2 . *Phys. Lett. B* **705**, 59–64 (2011). [doi:10.1016/j.physletb.2011.10.002](https://doi.org/10.1016/j.physletb.2011.10.002)
11. J. Arrington, I. Sick, Evaluation of the proton charge radius from electron–proton scattering. *J. Phys. Chem. Ref. Data* **44**, 031204 (2015). [doi:10.1063/1.4921430](https://doi.org/10.1063/1.4921430)
12. H world data corresponds to adjustment 8, table XXIX in (3).
13. R. Pohl, F. Nez, L. M. P. Fernandes, F. D. Amaro, F. Biraben, J. M. R. Cardoso, D. S. Covita, A. Dax, S. Dhawan, M. Diepold, A. Giesen, A. L. Gouvea, T. Graf, T. W. Hänsch, P. Indelicato, L. Julien, P. Knowles, F. Kottmann, E.-O. Le Bigot, Y.-W. Liu, J. A. M. Lopes, L. Ludhova, C. M. B. Monteiro, F. Mulhauser, T. Nebel, P. Rabinowitz, J. M. F. dos Santos, L. A. Schaller, K. Schuhmann, C. Schwob, D. Taqqu, J. F. C. A. Veloso, A. Antognini, CREMA Collaboration, Laser spectroscopy of muonic deuterium. *Science* **353**, 669–673 (2016). [doi:10.1126/science.aaf2468](https://doi.org/10.1126/science.aaf2468) [Medline](#)
14. B. de Beauvoir, C. Schwob, O. Acef, L. Jozefowski, L. Hilico, F. Nez, L. Julien, A. Clairon, F. Biraben, Metrology of the hydrogen and deuterium atoms: Determination of the Rydberg constant and Lamb shifts. *Eur. Phys. J. D* **12**, 61–93 (2000). [doi:10.1007/s100530070043](https://doi.org/10.1007/s100530070043)
15. B. de Beauvoir, C. Schwob, O. Acef, L. Jozefowski, L. Hilico, F. Nez, L. Julien, A. Clairon, F. Biraben, Erratum: *Eur. Phys. J. D* **12**, 61–93 (2000). [*Eur. Phys. J. D* **12**, 61–93 (2000)] *Eur. Phys. J. D* **14**, 398 (2001). [doi:10.1007/s100530170209](https://doi.org/10.1007/s100530170209)
16. D. J. Berkeland, E. A. Hinds, M. G. Boshier, Precise optical measurement of lamb shifts in atomic hydrogen. *Phys. Rev. Lett.* **75**, 2470–2473 (1995).
[doi:10.1103/PhysRevLett.75.2470](https://doi.org/10.1103/PhysRevLett.75.2470) [Medline](#)
17. Materials and methods are available as supplementary materials.
18. M. Horbatsch, E. A. Hessels, Shifts from a distant neighboring resonance. *Phys. Rev. A* **82**, 052519 (2010). [doi:10.1103/PhysRevA.82.052519](https://doi.org/10.1103/PhysRevA.82.052519)
19. D. J. Berkeland, thesis, Yale University (1995).
20. A. Marsman, M. Horbatsch, E. A. Hessels, The effect of quantum-mechanical interference on precise measurements of the $n = 2$ triplet P fine structure of helium. *J. Phys. Chem. Ref. Data* **44**, 031207 (2015). [doi:10.1063/1.4922796](https://doi.org/10.1063/1.4922796)

21. G.-P. Feng, X. Zheng, Y. R. Sun, S.-M. Hu, Laser-spectroscopy measurement of the fine-structure splitting 2^3P_1 – 2^3P_2 of ${}^4\text{He}$. *Phys. Rev. A* **91**, 030502 (2015). [doi:10.1103/PhysRevA.91.030502](https://doi.org/10.1103/PhysRevA.91.030502)
22. M. Horbatsch, E. A. Hessels, Shifts from a distant neighboring resonance for a four-level atom. *Phys. Rev. A* **84**, 032508 (2011). [doi:10.1103/PhysRevA.84.032508](https://doi.org/10.1103/PhysRevA.84.032508)
23. A. Marsman, M. Horbatsch, E. A. Hessels, Shifts due to neighboring resonances for microwave measurements of the 2^3P fine structure of helium. *Phys. Rev. A* **86**, 012510 (2012). [doi:10.1103/PhysRevA.86.012510](https://doi.org/10.1103/PhysRevA.86.012510)
24. A. Marsman, M. Horbatsch, E. A. Hessels, Shifts due to distant neighboring resonances for laser measurements of 2^3S_1 -to- 2^3P_J transitions of helium. *Phys. Rev. A* **86**, 040501 (2012). [doi:10.1103/PhysRevA.86.040501](https://doi.org/10.1103/PhysRevA.86.040501)
25. A. Marsman, E. A. Hessels, M. Horbatsch, Shifts due to quantum-mechanical interference from distant neighboring resonances for saturated fluorescence spectroscopy of the 2^3S to 2^3P intervals of helium. *Phys. Rev. A* **89**, 043403 (2014). [doi:10.1103/PhysRevA.89.043403](https://doi.org/10.1103/PhysRevA.89.043403)
26. D. C. Yost, A. Matveev, E. Peters, A. Beyer, T. W. Hänsch, T. Udem, Quantum interference in two-photon frequency-comb spectroscopy. *Phys. Rev. A* **90**, 012512 (2014). [doi:10.1103/PhysRevA.90.012512](https://doi.org/10.1103/PhysRevA.90.012512)
27. R. Loudon, *The Quantum Theory of Light* (Oxford Univ. Press, 1983).
28. U. D. Jentschura, P. J. Mohr, Nonresonant effects in one- and two-photon transitions. *Can. J. Phys.* **80**, 633–644 (2002). [doi:10.1139/p02-019](https://doi.org/10.1139/p02-019)
29. R. C. Brown, S. Wu, J. V. Porto, C. J. Sansonetti, C. E. Simien, S. M. Brewer, J. N. Tan, J. D. Gillaspy, Quantum interference and light polarization effects in unresolvable atomic lines: Application to a precise measurement of the ${}^{6,7}\text{Li}$ D_2 lines. *Phys. Rev. A* **87**, 032504 (2013). [doi:10.1103/PhysRevA.87.032504](https://doi.org/10.1103/PhysRevA.87.032504)
30. U. Fano, Effects of configuration interaction on intensities and phase shifts. *Phys. Rev.* **124**, 1866–1878 (1961). [doi:10.1103/PhysRev.124.1866](https://doi.org/10.1103/PhysRev.124.1866)
31. S. Schippers, Analytical expression for the convolution of a Fano line profile with a Gaussian. *Int. Rev. At. Mol. Phys.* **2**, 151–156 (2011).
32. S. Schippers, Analytical expression for the convolution of a Fano line profile with a Gaussian. [arXiv:1203.4281v2 \[physics.atom-ph\]](https://arxiv.org/abs/1203.4281v2) (13 May 2016).
33. A. Beyer, C. G. Parthey, N. Kolachevsky, J. Alnis, K. Khabarova, R. Pohl, E. Peters, D. C. Yost, A. Matveev, K. Predehl, S. Droste, T. Wilken, R. Holzwarth, T. W. Hänsch, M. Abgrall, D. Rovera, C. Salomon, P. Laurent, T. Udem, Precision spectroscopy of atomic hydrogen. *J. Phys. Conf. Ser.* **467**, 012003 (2013). [doi:10.1088/1742-6596/467/1/012003](https://doi.org/10.1088/1742-6596/467/1/012003)
34. A. Beyer, L. Maisenbacher, K. Khabarova, A. Matveev, R. Pohl, T. Udem, T. W. Hänsch, N. Kolachevsky, Precision spectroscopy of 2S – $n\text{P}$ transitions in atomic hydrogen for a new determination of the Rydberg constant and the proton charge radius. *Phys. Scr.* **T165**, 014030 (2015). [doi:10.1088/0031-8949/2015/T165/014030](https://doi.org/10.1088/0031-8949/2015/T165/014030)

35. A. Beyer, J. Alnis, K. Khabarova, A. Matveev, C. G. Parthey, D. C. Yost, R. Pohl, T. Udem, T. W. Hänsch, N. Kolachevsky, Precision spectroscopy of the 2S-4P transition in atomic hydrogen on a cryogenic beam of optically excited 2S atoms. *Ann. Phys.* **525**, 671–679 (2013). [doi:10.1002/andp.201300075](https://doi.org/10.1002/andp.201300075)
36. A. Beyer, L. Maisenbacher, A. Matveev, R. Pohl, K. Khabarova, Y. Chang, A. Grinin, T. Lamour, T. Shi, D. C. Yost, T. Udem, T. W. Hänsch, N. Kolachevsky, Active fiber-based retroreflector providing phase-retracing anti-parallel laser beams for precision spectroscopy. *Opt. Express* **24**, 17470–17485 (2016). [doi:10.1364/OE.24.017470](https://doi.org/10.1364/OE.24.017470) [Medline](#)
37. C. J. Sansonetti, C. E. Simien, J. D. Gillaspy, J. N. Tan, S. M. Brewer, R. C. Brown, S. Wu, J. V. Porto, Absolute transition frequencies and quantum interference in a frequency comb based measurement of the $^{6,7}\text{Li}$ D lines. *Phys. Rev. Lett.* **107**, 023001 (2011). [doi:10.1103/PhysRevLett.107.023001](https://doi.org/10.1103/PhysRevLett.107.023001) [Medline](#)
38. M. Horbatsch, E. A. Hessels, Tabulation of the bound-state energies of atomic hydrogen. *Phys. Rev. A* **93**, 022513 (2016). [doi:10.1103/PhysRevA.93.022513](https://doi.org/10.1103/PhysRevA.93.022513)
39. R. Pohl, F. Nez, T. Udem, A. Antognini, A. Beyer, H. Fleurbaey, A. Grinin, T. W. Hänsch, L. Julien, F. Kottmann, J. J. Krauth, L. Maisenbacher, A. Matveev, F. Biraben, Deuteron charge radius and Rydberg constant from spectroscopy data in atomic deuterium. *Metrologia* **54**, L1–L10 (2017). [doi:10.1088/1681-7575/aa4e59](https://doi.org/10.1088/1681-7575/aa4e59)
40. A. C. Vutha N. Bezginov, I. Ferchichi, M. C. George, V. Isaac, C. H. Storry, A. S. Weatherbee, M. Weel, E. A. Hessels, *Bull. Am. Phys. Soc.* **57**, D1.138 (2012)
41. S. Galtier, H. Fleurbaey, S. Thomas, L. Julien, F. Biraben, F. Nez, Progress in spectroscopy of the 1S–3S transition in hydrogen. *J. Phys. Chem. Ref. Data* **44**, 031201 (2015). [doi:10.1063/1.4922255](https://doi.org/10.1063/1.4922255)
42. D. C. Yost, A. Matveev, A. Grinin, E. Peters, L. Maisenbacher, A. Beyer, R. Pohl, N. Kolachevsky, K. Khabarova, T. W. Hänsch, T. Udem, Spectroscopy of the hydrogen 1S–3S transition with chirped laser pulses. *Phys. Rev. A* **93**, 042509 (2016). [doi:10.1103/PhysRevA.93.042509](https://doi.org/10.1103/PhysRevA.93.042509)
43. M. Puchalski, J. Komasa, P. Czachorowski, K. Pachucki, Complete $\alpha^6 m$ corrections to the ground state of H_2 . *Phys. Rev. Lett.* **117**, 263002 (2016). [doi:10.1103/PhysRevLett.117.263002](https://doi.org/10.1103/PhysRevLett.117.263002) [Medline](#)
44. J. Liu, E. J. Salumbides, U. Hollenstein, J. C. J. Koelemeij, K. S. E. Eikema, W. Ubachs, F. Merkt, Determination of the ionization and dissociation energies of the hydrogen molecule. *J. Chem. Phys.* **130**, 174306 (2009). [doi:10.1063/1.3120443](https://doi.org/10.1063/1.3120443) [Medline](#)
45. D. Sprecher, J. Liu, C. Jung, W. Ubachs, F. Merkt, Communication: The ionization and dissociation energies of HD. *J. Chem. Phys.* **133**, 111102 (2010). [doi:10.1063/1.3483462](https://doi.org/10.1063/1.3483462) [Medline](#)
46. J.-P. Karr, L. Hilico, J. C. J. Koelemeij, V. I. Korobov, Hydrogen molecular ions for improved determination of fundamental constants. *Phys. Rev. A* **94**, 050501 (2016). [doi:10.1103/PhysRevA.94.050501](https://doi.org/10.1103/PhysRevA.94.050501)

47. R. K. Altmann, S. Galtier, L. S. Dreissen, K. S. E. Eikema, High-precision Ramsey-comb spectroscopy at deep ultraviolet wavelengths. *Phys. Rev. Lett.* **117**, 173201 (2016). [doi:10.1103/PhysRevLett.117.173201](https://doi.org/10.1103/PhysRevLett.117.173201) [Medline](#)
48. U. D. Jentschura, P. J. Mohr, J. N. Tan, Fundamental constants and tests of theory in Rydberg states of one-electron ions. *J. Phys. B* **43**, 074002 (2010). [doi:10.1088/0953-4075/43/7/074002](https://doi.org/10.1088/0953-4075/43/7/074002)
49. M. Abramowitz, I. A. Stegun, Eds., *Handbook of Mathematical Functions: With Formulas, Graphs, and Mathematical Tables* (Courier Corporation, 1964), vol. 55.
50. C. Salomon, J. Dalibard, A. Aspect, H. Metcalf, C. Cohen-Tannoudji, Channeling atoms in a laser standing wave. *Phys. Rev. Lett.* **59**, 1659–1662 (1987). [doi:10.1103/PhysRevLett.59.1659](https://doi.org/10.1103/PhysRevLett.59.1659) [Medline](#)
51. F. Minardi, M. Artoni, P. Cancio, M. Inguscio, G. Giusfredi, I. Carusotto, Frequency shift in saturation spectroscopy induced by mechanical effects of light. *Phys. Rev. A* **60**, 4164–4167 (1999). [doi:10.1103/PhysRevA.60.4164](https://doi.org/10.1103/PhysRevA.60.4164)
52. C. Cohen-Tannoudji, in *Frontiers in Laser Spectroscopy*, Les Houches, Session XXVII, R. Balian, S. Haroche, and S. Liberman, Eds. (North-Holland Publishing Company, Amsterdam, 1977).
53. J. Dalibard, Y. Castin, K. Mølmer, Wave-function approach to dissipative processes in quantum optics. *Phys. Rev. Lett.* **68**, 580–583 (1992). [doi:10.1103/PhysRevLett.68.580](https://doi.org/10.1103/PhysRevLett.68.580) [Medline](#)
54. C. G. Parthey, thesis, Ludwig-Maximilians Universität München (2011).
55. I. I. Sobel'man, *An Introduction to the Theory of Atomic Spectra*, G. K. Woodgate, D. Ter Haar, Eds. (Pergamon Press, 1972), sect. 36.
56. A. W. Ali, H. R. Griem, Theory of resonance broadening of spectral lines by atom-atom impacts. *Phys. Rev.* **140**, A1044–A1049 (1965). [doi:10.1103/PhysRev.140.A1044](https://doi.org/10.1103/PhysRev.140.A1044)
57. N. Kolachevsky, J. Alnis, C. G. Parthey, A. Matveev, R. Landig, T. W. Hänsch, Low phase noise diode laser oscillator for 1S-2S spectroscopy in atomic hydrogen. *Opt. Lett.* **36**, 4299–4301 (2011). [doi:10.1364/OL.36.004299](https://doi.org/10.1364/OL.36.004299) [Medline](#)
58. J. Alnis, A. Matveev, N. Kolachevsky, T. Udem, T. W. Hänsch, Subhertz linewidth diode lasers by stabilization to vibrationally and thermally compensated ultralow-expansion glass Fabry-Pérot cavities. *Phys. Rev. A* **77**, 053809 (2008). [doi:10.1103/PhysRevA.77.053809](https://doi.org/10.1103/PhysRevA.77.053809)
59. N. Kolachevsky, A. Matveev, J. Alnis, C. G. Parthey, S. G. Karshenboim, T. W. Hänsch, Measurement of the 2S hyperfine interval in atomic hydrogen. *Phys. Rev. Lett.* **102**, 213002 (2009). [doi:10.1103/PhysRevLett.102.213002](https://doi.org/10.1103/PhysRevLett.102.213002) [Medline](#)